Journal of the Mechanics and Physics of Solids 105 (2017) 131–149

Contents lists available at ScienceDirect

Journal of the Mechanics and Physics of Solids

journal homepage: www.elsevier.com/locate/jmps

Geometrically necessary dislocation density measurements at a grain boundary due to wedge indentation into an aluminum bicrystal

C.F.O. Dahlberg[a,*], Y. Saito[b], M.S. Öztop[b], J.W. Kysar[b]

[a] *Department of Solid Mechanics, School of Engineering Sciences, Royal Institute of Technology (KTH), Teknikringen 8D, SE-100 44 Stockholm, Sweden*

[b] *Department of Mechanical Engineering, Fu Foundation School of Engineering and Applied Science, Columbia University, 500 West 120th Street, New York, NY 10027, USA*

ARTICLE INFO

Article history:
Received 2 November 2016
Revised 19 April 2017
Accepted 11 May 2017
Available online 12 May 2017

Keywords:
Geometrically necessary dislocation density
Indentation
Crystal plasticity
Grain boundary
Bicrystal

ABSTRACT

An aluminum bicrystal with a symmetric tilt $\Sigma 43\,(3\,3\,5)[1\,1\,0]$ coincident site lattice grain boundary was deformed plastically via wedge indentation under conditions that led to a plane strain deformation state. Plastic deformation is induced into both crystals and the initially straight grain boundary developed a significant curvature. The resulting lattice rotation field was measured via Electron Backscatter Diffraction (EBSD). The Nye dislocation density tensor and the associated Geometrically Necessary Dislocation (GND) densities introduced by the plastic deformation were calculated. The grain boundary served as an impediment to plastic deformation as quantified through a smaller lattice rotation magnitude and smaller GND density magnitudes in one of the crystals. There is evidence that the lattice rotations in one grain brought a slip system in that grain into alignment with a slip system in the other grain, upon which the impediment to dislocation transmission across the grain boundary was reduced. This allowed the two slip systems to rotate together in tandem at later stages of the deformation. Finite element crystal plasticity simulations using classical constitutive hardening relationship capture the general features observed in the experiments.

1. Introduction

The motion and multiplication of dislocations are the mechanisms responsible for plastic deformation in most metals at quasistatic deformation rates. The qualitative behavior of dislocations in single crystals or individual grains of a metal is generally understood in terms of the physical mechanisms and interactions of dislocations, although a predictive quantitative understanding remains elusive (e.g. McDowell, 2010). Polycrystalline metals typically have significantly different responses than single crystals due to the presence of grain boundaries. The mechanics and physics of interactions between dislocations and grain boundaries are much more complicated than intragranular dislocation interactions alone. Indeed the qualitative behavior of the various physical mechanisms and interactions of dislocations near grain boundaries is not yet well understood, let alone a quantitative behavior (e.g. Bieler et al., 2014; Spearot and Sangid, 2014).

* Corresponding author.
E-mail address: carldahl@kth.se (C.F.O. Dahlberg).

http://dx.doi.org/10.1016/j.jmps.2017.05.005

In this study we characterize the plastic deformation in an aluminum bicrystal. The mechanical testing of bicrystals to infer the properties of grain boundaries has a long history. Some early work on aluminum bicrystals can be found in Clark and Chalmers (1954), Aust and Chen (1954), Livingston and Chalmers (1957) and Davis et al. (1966) where stress-strain tensile test data are correlated to known orientations of a single grain boundary. Similar tests by Davis et al. (1966), Miura and Saeki (1978), Rey and Zaoui (1980) and Lim and Raj (1985) observed slip lines on the specimen surface close to the grain boundary to investigate grain boundary mechanics. With the introduction of Orientation Imaging Microscopy (OIM) via Electron Backscatter Diffraction (EBSD) with micrometer-scale spatial resolution, the mechanical response can be coupled to the complete determination of crystal orientations. Examples of this technique can be found in Sun et al. (2000), Larson et al. (2004), Okada et al. (2006), Zaeffer et al. (2003) and Ohashi et al. (2009). A recent study of grain boundary properties using nanoindentation can be found in Wang and Ngan (2004), Soer and De Hosson (2005) and Vachhani et al. (2016). Finally, several studies have investigated the behavior of dislocations near the tips of cracks that lie along grain boundaries, including Kysar (2000, 2001a, 2001b) as well as Kysar and Briant (2002).

The specimen employed in this study is a bicrystal of face-centered cubic (FCC) aluminum. The grain boundary has a symmetric tilt character with a shared tilt axis parallel to the [110] direction of both crystals. As will be described in more detail below, the grain boundary abuts a plane from the {335} family of atomic planes in both crystals. If the crystallographic lattice of one crystal were to be extended mathematically into the lattice of the other crystal, 1/43 of the lattice sites would coincide. Hence, this grain boundary is designated as a Coincident Site Lattice (CSL) $\Sigma 43(3\,3\,5)[1\,1\,0]$.

The mechanical loading on the bicrystal, the orientation of the grain boundary, the specimen configuration, and the crystallographic orientations of the grains are chosen or prescribed to induce a plane strain elastic-plastic deformation state in the material near and within the grain boundary. Plastic slip occurs on three pairs of active slip systems in each crystal; two are coplanar pairs and the third is a collinear pair. Each pair of slip systems together acts as an effective in-plane (i.e. plane strain) slip system. In the sequel we discuss the plastic deformation in terms of the three effective in-plane slip systems. The plane strain plastic deformation is induced in the specimen via a wedge indenter with a 90° included angle. The plastically deforming zone straddles the grain boundary and extends into both grains. Thus our experimental measurements are designed to give insight into how dislocations interact with the grain boundary during plastic deformation under plane strain conditions.

We measure the crystal lattice rotation induced by the plane strain plastic deformation via the method of Electron Backscatter Diffraction (EBSD) in a Scanning Electron Microscope (SEM). From these measurements, we calculate the Nye dislocation density tensor as well as the Geometrically Necessary Dislocation (GND) density on each of the three effective in-plane plastic slip systems using methods developed in Kysar et al. (2010) and Dahlberg et al. (2014).

The stress and deformation states associated with wedge indentation into single crystals have been analyzed in detail both with analytical and numerical methods in Saito and Kysar (2011), Saito et al. (2012) and Dahlberg et al. (2014). In this study we extend those analyses to wedge indentation into bicrystals via detailed single crystal plasticity finite element simulations.

The lattice rotation field predicted from the simulations is largely consistent with experimental measurements. We focus attention on a pair of coplanar slip systems that exist in each grain and intersect at the grain boundary; the two slip planes are nearly parallel prior to deformation. The GND density measurements suggest that the grain boundary impeded dislocation motion causing dislocations to pile up against the grain boundary at the initial stages of the deformation. However as deformation proceeds, lattice rotation in one grain brings the coplanar slip system in that grain into alignment with the coplanar slip system in the other grain, upon which the impediment to dislocation transmission across the grain boundary diminishes. As further deformation occurs, the two coplanar pairs of slip systems rotate in tandem suggesting that the grain boundary becomes largely transparent to the transmission of dislocations.

The paper is organized as follows. Section 2 reviews the geometry and relevant variables associated with plastic slip transmission across a grain boundary. In addition, the various proposed mechanisms and criteria of plastic slip transmission across a grain boundary are reviewed. Section 3 discusses the test specimen, the experimental procedures, data collection and data processing. In Section 4 the experimental results are presented and analyzed with respect to lattice rotations and densities of geometrically necessary dislocations. Section 5 discusses detailed finite element method crystal plasticity simulations of the experiment. The simulation results are compared to the experimental results both qualitatively and quantitatively. The results are discussed in Section 6 and conclusions are drawn in Section 7.

2. Background

We now review the geometry and notation for general grain boundaries and plastic slip systems. The idealized geometry of a grain boundary and its two adjoining crystals (also referred to as grains) is shown in Fig. 1. Adopting the terminology of Mercier et al. (2016), the *incoming slip plane* in crystal #1 has unit normal vector $\boldsymbol{n}_{\mathrm{in}}$ with Burgers vector $\boldsymbol{b}_{\mathrm{in}}$. The *outgoing slip plane* in crystal #2 has unit normal vector $\boldsymbol{n}_{\mathrm{out}}$ with Burgers vector $\boldsymbol{b}_{\mathrm{out}}$. The angle between $\boldsymbol{n}_{\mathrm{in}}$ and $\boldsymbol{n}_{\mathrm{out}}$ is denoted by ψ. The intersection of the incoming slip plane and the grain boundary plane is denoted by the line $\boldsymbol{l}_{\mathrm{in}}$ and the intersection of the outgoing slip plane and the grain boundary is denoted by the line $\boldsymbol{l}_{\mathrm{out}}$. In general $\boldsymbol{l}_{\mathrm{in}}$ and $\boldsymbol{l}_{\mathrm{out}}$ meet at one point and the angle between them is denoted as θ. The unit vector $\boldsymbol{d}_{\mathrm{in}}$ indicates the direction of the prolongation of $\boldsymbol{b}_{\mathrm{in}}$ from crystal #1 (through the intersection of $\boldsymbol{l}_{\mathrm{in}}$ and $\boldsymbol{l}_{\mathrm{out}}$) into crystal #2. For consistency, the unit vector $\boldsymbol{d}_{\mathrm{out}}$ indicates the direction of

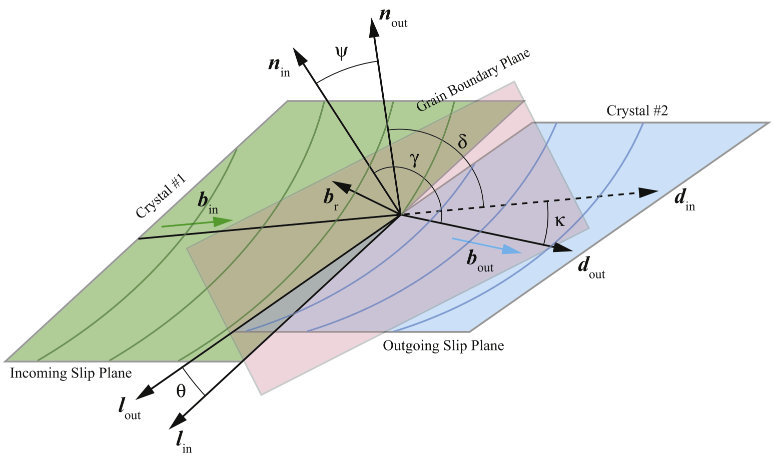

Fig. 1. Schematic diagram of grain boundary with intersecting dislocation slip planes, following Mercier et al. (2016).

the prolongation of $\boldsymbol{b}_{\mathrm{out}}$ within crystal #2 with origin at the intersection between $\boldsymbol{l}_{\mathrm{in}}$ and $\boldsymbol{l}_{\mathrm{out}}$. The angle between $\boldsymbol{d}_{\mathrm{in}}$ and $\boldsymbol{d}_{\mathrm{out}}$ is denoted by κ. The angle between $\boldsymbol{b}_{\mathrm{out}}$ and $\boldsymbol{n}_{\mathrm{in}}$ is denoted as γ. The angle between $\boldsymbol{b}_{\mathrm{in}}$ and $\boldsymbol{n}_{\mathrm{out}}$ is denoted as δ.

If crystal #1 and crystal #2 are the same material and phase and the incoming and outgoing slip systems are of the same crystallographic family, the grain boundary has pure tilt character when $\boldsymbol{l}_{\mathrm{in}}$ coincides with $\boldsymbol{l}_{\mathrm{out}}$; the tilt angle is denoted as ψ. Furthermore the grain boundary has *symmetric* tilt character when the sum of $\boldsymbol{n}_{\mathrm{in}}$ and $\boldsymbol{n}_{\mathrm{out}}$ lies in the plane of the grain boundary.

Treatment of the grain boundary as a plane does not account for its atomic complexity. It has been understood since Taylor (1934), Burgers (1939) and Bragg (1940) that grain boundaries can be considered as arrays of dislocations. Further Read and Shockley (1950) and Frank (1951) considered grain boundaries in terms of the energies of the dislocation arrays in grain boundaries. Hence even for idealized planar grain boundaries the atomic structures at the transition between two grains are not confined to a single atomic plane. Atomic scale simulations methods such as Density Functional Theory (DFT) and Molecular Dynamics (MD) have given significant insight into the possible atomic scale configurations of grain boundaries (e.g. Tschopp and McDowell, 2007; Tschopp et al., 2015). Additional complexities arise when the grain boundary is not planar (Smith and Farkas, 2016; Van Swygenhoven et al., 2000).

We now review the plastic slip transmission mechanisms and related criteria. Dislocations have at least three classes of interactions with grain boundaries (e.g. Bayerschen et al., 2016). First, the grain boundary can serve as a source—i.e. a nucleation mechanism—for dislocations, especially in nanocrystalline materials (e.g. Van Swygenhoven and Weertman, 2006) where bulk dislocation sources can not operate. Second, a grain boundary can act as a sink—i.e. an impenetrable barrier—to dislocation motion, with the dislocations either piling up against the grain boundary or being incorporated into the grain boundary itself and thereby changing the grain boundary atomic structure (Eshelby et al., 1951; Hall, 1951; Petch, 1953). This occurs most readily with high angle grain boundaries. Third, a dislocation can allow plastic slip to *transmit* from one crystal to another through the grain boundary (e.g. Lim and Raj, 1985; Kacher et al., 2014).

Plastic slip can be transmitted across a grain boundary, such as in Fig. 1, via three different mechanisms (e.g. Sutton and Balluffi, 1995; Bayerschen et al., 2016). First, dislocation transmission can occur directly across the grain boundary if the Burgers vectors of the incoming and outgoing slip systems coincide. Under this set of conditions the grain boundary would pose little to no barrier to dislocation motion. Second, dislocation transmission can occur directly across the grain boundary with incoming and outgoing slip systems having different Burgers vectors which results in a *residual* Burgers vector, $\boldsymbol{b}_{\mathrm{r}}=\boldsymbol{b}_{\mathrm{in}}-\boldsymbol{b}_{\mathrm{out}}$, in the grain boundary as shown schematically in Fig. 1. The line of the residual dislocation will lie in the grain boundary but $\boldsymbol{b}_{\mathrm{r}}$ will not in general lie in the plane of the grain boundary. The grain boundary poses a partial barrier to the dislocation motion thus requiring a larger resolved shear stress to effect the transmission of plastic slip. In addition elastic line energy associated with the residual Burgers vector increases the resistance to transmission of plastic slip. Third, the grain boundary can serve as a barrier to the direct transmission of dislocations, but the resulting pile up of dislocations on the incoming slip system at the grain boundary can nucleate dislocation sources on the outgoing slip system. This mechanism poses a large barrier to the transmission of plastic slip. The line energy associated with the residual Burgers vector in the grain boundary further increases slip resistance across the grain boundary.

A recent paper by Bayerschen et al. (2016) reviews the criteria for the transmission of plastic slip across a grain boundary. The criteria can be categorized in three different classes. The first accounts for various *geometrical effects* alone. Examples include the *N*-factor criterion by Livingston and Chalmers (1957), the *LRB*-factor criterion by Shen et al. (1986); 1988), the m'-factor by Wang and Ngan (2004) as well as Wo and Ngan (2004), minimization of the $\boldsymbol{b}_{\mathrm{r}}$ magnitude by Marcinkowski and Tseng (1970) and Bollmann (1970), consideration of the overall misorientation of the two crystals by Aust and Chen (1954) and Clark and Chalmers (1954), and the λ-factor by Werner and Prantl (1990), among other criteria. The second set

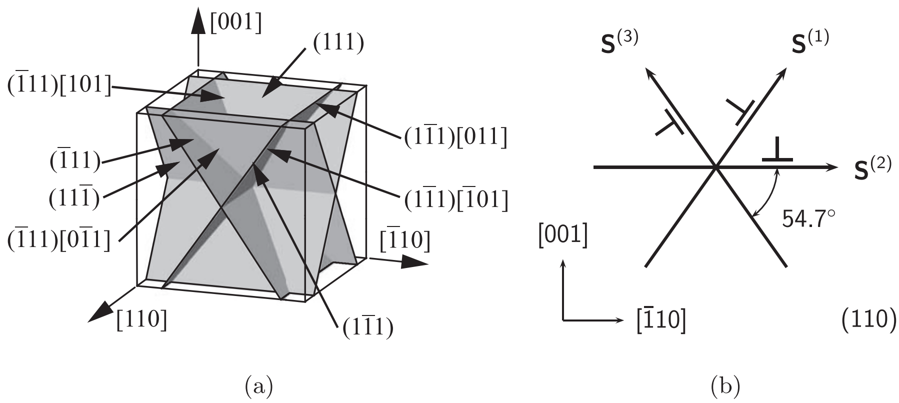

Fig. 2. Crystallography of face-centered cubic crystal: (a) Illustration of crystallographic slip systems relative to wire-frame representing specimen edges; (b) Orientation of mth effective plane strain slip system (for $m = 1, 2, 3$) denoted by in-plane effective unit slip direction $\boldsymbol{S}^{(m)}$, with the sense of a positive effective edge dislocation on slip system indicated.

of criteria account for *stress effects* alone. Examples include maximizing the sum of the maximum Schmid factors in the incoming and outgoing grains as in Reid and Owen (1973) and Abuzaid et al. (2012), a Generalized Schmid Factor (GSF) criterion by Reid and Owen, 1973 and Bieler et al., 2014, as well as maximizing the resolved shear stress on the outgoing slip system from the piled up dislocations at the grain boundary on the incoming slip system by Lee et al. (1989); 1990) and Clark et al. (1992). A third set of criteria account for both geometrical and stress effects. For example, Bieler et al. (2014) considered both a geometric parameter for slip transfer as well as the local stress state. Another example is Tsuru et al. (2016) who also accounted for the angular disorientation of the two slip systems along with the applied stress.

3. Experiments

In this Section we discuss the crystallography of the plastic slip systems, the specimen preparation and mechanical loading, the spatially resolved EBSD measurements as well as the methodology to determine the GND densities.

3.1. Effective in-plane plastic slip systems

For FCC crystals under a plane strain deformation state in the (1 1 0) crystallographic plane, Rice (1987) demonstrated that only six of the twelve slip systems in the $\{1\,1\,1\}\langle 1\,1\,0\rangle$ family of slip systems, shown in Fig. 2a, are activated. Furthermore the six active slip systems are activated as three pairs of slip systems whereby each pair induces plastic deformation with effective slip direction within the plane of plane strain. Rice (1987) referred to each of these pairs of slip systems as an effective in-plane (or plane strain) slip system.

Following Kysar et al. (2005), Gan et al. (2006), Gan and Kysar (2007), Kysar et al. (2007) and Kysar et al. (2010) and as shown in Fig. 2b, we label the effective in-plane slip systems arbitrarily as slip systems 1, 2 and 3. Plastic deformation on effective in-plane slip system 2 occurs via the activation of a pair of collinear slip systems that collectively introduce slip in the direction of unit vector $\boldsymbol{S}^{(2)}$. Plastic deformation on each of the effective in-plane slip systems 1 and 3 occurs via the activation of a pair of coplanar slip systems that collectively introduce slip in the direction, respectively, of unit vector $\boldsymbol{S}^{(1)}$ and $\boldsymbol{S}^{(3)}$; these effective in-plane slip directions have mirror symmetry about the [0 0 1] crystallographic direction. The angle between $\boldsymbol{S}^{(1)}$ and $\boldsymbol{S}^{(2)}$ is $\tan^{-1}(\sqrt{2}) \approx 54.7356°$.

3.2. Specimen preparation

The aluminum in the specimen is at least 99.9999% pure. The first preparation step was to grow a single crystal using the seeded Bridgman–Stockbarger technique in a high purity graphite crucible. After etching the resulting single crystal in NaOH to remove the native oxide layer formed during crystal growth, the orientation of the crystal was determined by Laue x-ray diffraction to within ± 0.5°. A wire electrical discharge machine (EDM) was used to cut the crystal into two parallelepiped seeds (3 × 5 × 40 mm) for subsequent growth of the bicrystal. The longitudinal axis of the seeds coincided with the [$\bar{5}$ 5 6] crystallographic direction. One of the 5 × 40 mm surfaces coincided with the (1 1 0) crystallographic plane. One of the 3 × 40 mm surfaces coincided with the (3 $\bar{3}$ 5) crystallographic plane. As described in the Appendix, one of the crystal seeds was subsequently rotated 180° about its longitudinal axis and both seeds were placed within a graphite crucible for growth of the bicrystal via the Bridgman–Stockbarger technique. Thus the bicrystal contains a symmetric tilt $\Sigma 43\,(3\,3\,5)[1\,1\,0]$ coincident site lattice (CSL) grain boundary.

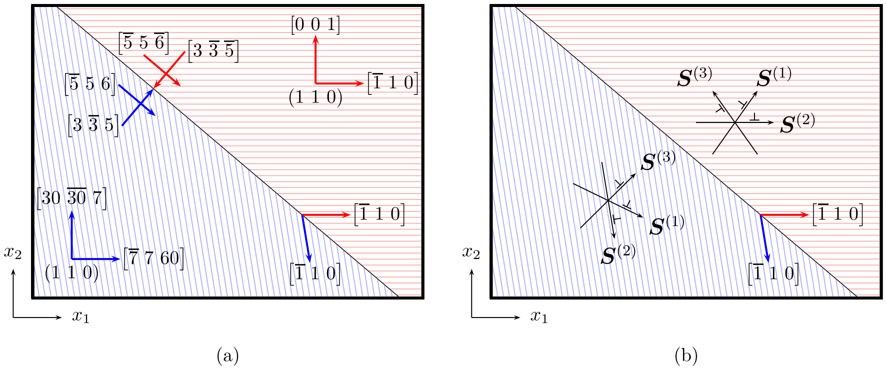

Fig. 3. Crystallographic orientation of aluminium bicrystal in the (110)-plane: (a) Miller indices show orientation of both crystals; (b) Orientations of three effective in-plane slip systems.

Previous experiments (e.g. Dahlberg et al., 2014; Kysar et al., 2010) to characterize plastic deformation in FCC single crystals employed specimens with $[\bar{1}\,1\,0]$ parallel to the x_1-axis, $[0\,0\,1]$ parallel to the x_2-axis and $[1\,1\,0]$ parallel to the out-of-plane x_3-axis in the undeformed state. The specimen in this study was excised from the bicrystal such that one of the crystals had the same orientation relative to the specimen coordinate frame as in the single crystal experiments; we refer to this as the “right” crystal or grain due to its position relative to the grain boundary, as can be seen in Fig. 3.

The specimen was loaded via wedge indentation into the right crystal so we expect the deformation fields in the right crystal to share many of the characteristics that have already been well documented and analyzed in the previous studies. The “left” crystal or grain had crystallographic orientation most conveniently expressed as having $[\bar{7}\,7\,60]$ parallel to the x_1-axis, $[30\,\overline{30}\,7]$ parallel to the x_2-axis and [110] parallel to the out-of-plane x_3-axis. As seen in Fig. 3a, the angle between the grain boundary and the $[\bar{1}\,1\,0]$ direction of each crystal is $\cos^{-1}(5/\sqrt{43}) \approx 40.3155^\circ$.

The three effective in-plane slip systems are shown in Fig. 3b for each crystal within the bicrystal. In the right crystal they are oriented exactly as in Fig. 2b so that $\boldsymbol{S}^{(1)}$ is oriented at an angle of $\tan^{-1}(\sqrt{2}) \approx 54.7356^\circ$ relative to the specimen x_1-axis. In the left crystal, the effective in-plane slip direction $\boldsymbol{S}^{(3)}$ is oriented at an angle of $\cos^{-1}(53/43\sqrt{3}) \approx 44.6333^\circ$ to the specimen x_1-axis. The positive sense of the effective in-plane edge dislocations on each of the effective slip systems is shown in Fig. 3b.

In an undeformed bicrystal, the direction of $\boldsymbol{S}^{(3)}$ in the left crystal and $\boldsymbol{S}^{(1)}$ in the right crystal differ by 10.1023°. Both effective in-plane slip systems consist of coplanar pairs of slip systems. Hence this combination of effective in-plane slip systems offers the opportunity to investigate the possibility of interactions of dislocations with the grain boundary as well as the possibility of the transmission of plastic slip across a grain boundary. We will focus on this pair of effective slip systems in the discussion below.

3.3. Specimen loading and OIM surface preparation

Fig. 4 shows a schematic illustration of the indentation experiment. The wedge indenter was made of tungsten carbide (WC) bonded by a ferrous alloy and cut to shape via EDM to have an included angle of 90°. The indenter tip was positioned on the $(0\,0\,1)$ surface of the right grain with the axis of the wedge parallel to the $[1\,1\,0]$ direction. The indenter tip was approximately 350 µm away from the grain boundary as seen in Fig. 4a. The indentation process occurred under displacement control using a universal mechanical testing system (MTS 810 with a 548 controller). The wedge indenter impinged into the right crystal in the $[0\,0\,\bar{1}]$ direction to a depth of about 200 µm shown schematically in Fig. 4b. During indentation, the load and the indentation penetration displacement data were recorded. A plot of force/length (i.e. normalized by the length of the wedge in contact with the bicrystal) as a function of indentation depth is shown in Fig. 5.

The extent of the plastically deformed region below the indenter tip is much smaller than any other characteristic length related to the specimen, except the distance from the indenter to the grain boundary. Thus *small scale yielding* (Rice, 1968) ensures that the plastically deformed zone is surrounded by a much larger region of elastic deformation, that constrains the plastic deformation state to be one of plane strain in the $(1\,1\,0)$ planes of both grains of the bicrystal in this specimen. However the conditions necessary to ensure plane strain deformation (Kysar et al., 2005; Rice, 1987) are not satisfied on the lateral surfaces (i.e. both specimen surfaces with normals aligned with the x_3-axis in Fig. 4a) of the specimen. Thus, after indentation, the midsection of the bicrystal was cut by wire EDM as shown in Fig. 4c to expose a $(1\,1\,0)$ surface that suffered plane strain plastic deformation (Kysar et al., 2010).

After the initial EDM cut, the exposed surface was smoothened with four skim cuts each with progressively less power to reduce the thickness of the damage layer induced by the EDM. The indented surface was then coated with lacquer (SPI Supplies, West Chester, PA) and the newly exposed $(1\,1\,0)$ surface of the bicrystal specimen was electropolished in an electrolyte containing 30% nitric acid and 70% methyl alcohol (by volume) at a temperature of −20°C. The exposed surface

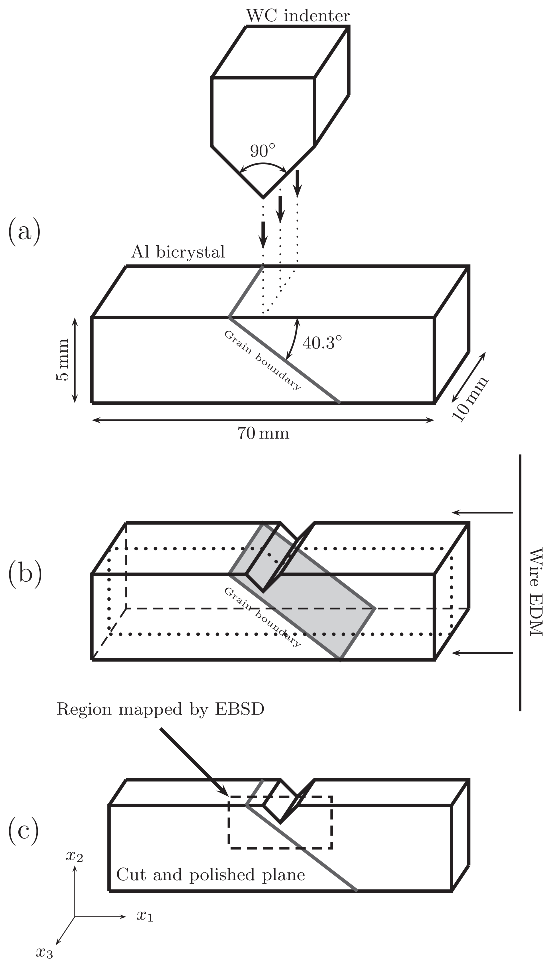

Fig. 4. Sketch of experimental procedure. (a) Initial geometry of Al bicrystal specimen and orientation of the grain boundary and indication of how the wedge indenter was applied; (b) Indented specimen was cut by wire EDM to expose a plane that had suffered plane strain deformation; (c) Exposed plane was polished and a region of approximately 1000 µm × 800 µm was mapped by EBSD.

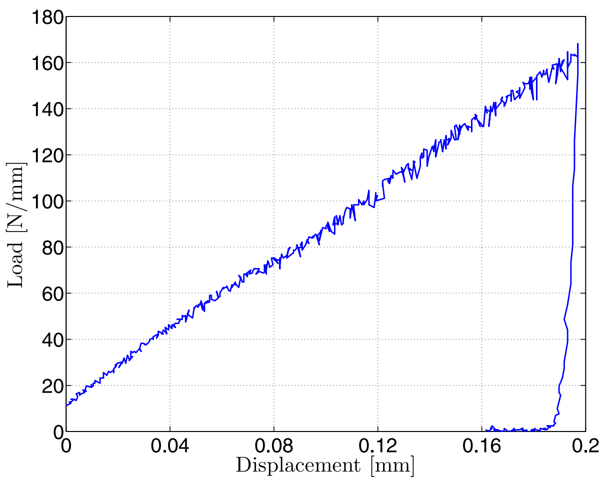

Fig. 5. Force per unit width (N/mm) vs. indentation depth (mm) during the indentation process.

was connected to the anode and located 5 mm away from the cathode in the electrochemical cell. A constant current of 0.1 A was applied for 30 min. The lacquer was removed after electropolishing and the specimen was ultrasonically cleaned with deionized water to remove any adhering particles.

3.4. Electron backscatter diffraction analysis

The as-deformed orientation of the crystal lattice on the newly exposed surface was measured with EBSD on a JEOL 5600 SEM. A Si single crystal was used for detector orientation and projection parameter calibration. Following calibration, the Kikuchi diffraction patterns were obtained at a 20 kV accelerating voltage at working distance of 12 mm. The measurements were made on a 3 µm square raster over an area of about 1 × 1 mm.

3.5. Determination of GND densities

The Kikuchi diffraction patterns were processed with HKL Channel 5 software to determine the as-deformed crystallographic orientation of the specimen in terms of Euler angles at each measurement position. The overall experimental uncertainty of the angular orientation is about ± 0.5° as discussed in Gardner et al. (2011). The Euler angles do not represent a unique lattice configuration because of the symmetries in the FCC crystal lattice. Thus an algorithm based on quaternion algebra, similar in spirit to work by Gupta and Agnew (2010), was implemented in Matlab to post-process the Euler angle data and determine the crystallographic orientation in the deformed configuration. The lattice rotation was determined at each measurement point by comparing the measured as-deformed crystallographic orientation with the known crystallographic orientation of the undeformed crystal lattice. By using quaternions to describe the rotation it is straightforward to decompose the lattice rotation into out-of-plane and in-plane components. As reported in Kysar et al. (2010), the in-plane lattice rotation (i.e. rotation about the out-of-plane x_3-axis coinciding with [1 1 0]) denoted as ω_3 is at least one order of magnitude larger than the out-of-plane lattice rotation components about the in-plane x_1-axis and x_2-axis, which validates our assumption of plane strain plastic deformation. Thus in what follows we treat ω_3 as the only non-zero lattice rotation component.

Adopting small-strain kinematics, the lattice curvature tensor, κ_{ij}, is calculated from the lattice rotation ω_i about the x_i-axis as

$$\kappa_{ij} = \frac{\partial \omega_i}{\partial x_j}. \tag{1}$$

Nye's dislocation density tensor (Arsenlis and Parks, 1999; Nye, 1953) is calculated as

$$\alpha_{ji} = -\kappa_{ij} + \kappa_{kk}\delta_{ij} + e_{ipk}\frac{\partial \varepsilon^{\mathrm{el}}_{jk}}{\partial x_p}. \tag{2}$$

where $\varepsilon^{\mathrm{el}}_{jk}$ is the elastic strain of the crystal lattice. For a plane strain deformation state, the lattice curvature tensor and the Nye tensor each have only two non-zero components; specifically only the κ_{31} and κ_{32} components as well as the α_{13} and α_{23} components are non-zero. As discussed in Kysar et al. (2010), we determine experimentally both non-zero components of the lattice curvature tensor by taking numerical derivatives of the ω_3 with respect to x_1 and x_2 while neglecting ω_1 and ω_2. In addition we neglect the lattice strain in the third term in Eq. (2). Thus, both non-zero Nye tensor components can be determined from the measured lattice rotation. After calculating the two non-zero Nye tensor components we express them in a local coordinate frame in the rotated crystal lattice such that the local x'_1-axis is parallel to the local $[\bar{1}\,1\,0]$ direction, the local x'_2-axis is parallel to the local [0 0 1] direction and the local x_3-axis remains parallel to the out-of-plane [1 1 0] direction. As discussed in Kysar et al. (2010), the Nye tensor components can be expressed as $\alpha'_{13} = \alpha_{13}\cos\omega_3 + \alpha_{23}\sin\omega_3$ and $\alpha'_{23} = -\alpha_{13}\sin\omega_3 + \alpha_{23}\cos\omega_3$.

The Nye tensor is in turn directly related to the weighted sum of GND densities on all slip systems as

$$\alpha_{ij} = \sum_{m=1}^{N_e} \rho^{(m)}_{\mathrm{gnd(e)}} b^{(m)} s^{(m)}_i t^{(m)}_j + \sum_{m=1}^{N_s} \rho^{(m)}_{\mathrm{gnd(s)}} b^{(m)} s^{(m)}_i s^{(m)}_j \tag{3}$$

where N_e and N_s are the number of unique edge and screw dislocation components in the crystal, $\rho^{(m)}_{\mathrm{gnd(e)}}$ and $\rho^{(m)}_{\mathrm{gnd(e)}}$ are edge and screw components, respectively, of the GND density on slip system m, and $b^{(m)}$ is the magnitude of Burgers vector. Furthermore, $\boldsymbol{n}^{(m)}$ and $\boldsymbol{s}^{(m)}$ are the unit slip plane normal vector and unit slip direction vector, respectively, on slip system m, and $\boldsymbol{t}^{(m)} = \boldsymbol{s}^{(m)} \times \boldsymbol{n}^{(m)}$.

Strictly speaking Eqs. (2) and (3) are valid only for small-strain kinematics. As will be seen below, lattice rotations about the out-of-plane axis can be as large as 20° which apparently violate the small-strain assumptions. However Kysar et al. (2010) discussed that the small-strain kinematic analysis is still valid for the plane strain deformation case because lattice rotations occur only about one axis.

In this study we treat all plastic deformation as being due to three in-plane effective edge dislocation slip systems. Thus, as in Kysar et al. (2010), Eq. (3) reduces to

$$\alpha_{ij} = \sum_{m=1}^{N_e} \rho_{\text{gnd}}^{(m)} b^{(m)} s_i^{(m)} t_j^{(m)} \tag{4}$$

where $N_e = 3$ and $\rho_{\text{gnd}}^{(m)}$ refers to the effective edge slip systems shown in Fig. 2b where the positive sense of the effective edge dislocations is also indicated. Thus Eq. (4) relates the GND densities on the three effective slip planes in Fig. 2b to the two experimentally measured non-zero Nye dislocation tensor components. For the FCC crystal specimen considered herein, there results the system of equations

$$\begin{bmatrix} \alpha'_{13} \\ \alpha'_{23} \end{bmatrix} = \begin{bmatrix} \frac{\sqrt{3}}{4} & \frac{1}{\sqrt{3}} & -\frac{\sqrt{3}}{4} \\ \frac{\sqrt{6}}{4} & 0 & \frac{\sqrt{6}}{4} \end{bmatrix} \begin{bmatrix} \rho_{\text{gnd}}^{(1)} b^{(1)} \\ \rho_{\text{gnd}}^{(2)} b^{(2)} \\ \rho_{\text{gnd}}^{(3)} b^{(3)} \end{bmatrix} \tag{5}$$

derived in Kysar et al. (2010). This system of equations is under-determined so that an infinity of solutions exist. Thus as proposed by Arsenlis and Parks (1999) and Kysar et al. (2010) defined an L^1-norm of the GND densities as

$$\rho_{\text{gnd}}^{\text{tot}} = \left|\rho_{\text{gnd}}^{(1)}\right| + \left|\rho_{\text{gnd}}^{(2)}\right| + \left|\rho_{\text{gnd}}^{(3)}\right| \tag{6}$$

which has the physical interpretation of being the *total GND density*. Upon minimizing $\rho_{\text{gnd}}^{\text{tot}}$ subject to Eq. (5), Kysar et al. (2010) derived an analytic solution for the *lower bound on total GND density*, which is the minimum total GND density necessary to transform an undeformed crystal lattice into the measured crystal lattice configuration.

It is common to find regions of the plastically deformed bicrystal where only one or two effective in-plane slip systems have been activated. Under those conditions the GND density associated with the inactive slip systems can be set to zero *a priori*, which removes the under-determined character of Eq. (5) and allows the actual (and unique) solution of the remaining GND densities to be found.

Interestingly, the lower bound solution reduces to the actual solution whenever an actual solution exists. Hence in what follows we calculate the lower bound solution from the measured Nye tensor components and subsequently interpret the results by determining whether the results correspond to the actual solution. Both the lower bound solution and the actual solution can be expressed either in terms of the total GND density or the apportionment of the total GND density onto the individual effective slip systems.

Finally we review the physical meaning of the Nye dislocation density tensor. A tensor transforms one vector quantity into another. The Nye dislocation density tensor, α, transforms a unit vector $\boldsymbol{m}$ that denotes a direction in a crystal lattice into a vector $\boldsymbol{B}$ that represents the net Burgers vector of all dislocations on a per unit area basis within a Burgers circuit taken about the $\boldsymbol{m}$ axis according to the right-hand rule. This is expressed mathematically as

$$\boldsymbol{B} = \alpha \cdot \boldsymbol{m} \tag{7}$$

where $\boldsymbol{B}$ is referred to as the *net Burgers density vector* (or, equivalently, the net closure failure density vector). Its magnitude has units of inverse length (i.e. length per area). The tensor transformation in Eq. (7) represents the continuum manifestation of the Burgers circuit in a discrete lattice. For the plane strain Nye tensor with two non-zero components and upon choosing $\boldsymbol{m}$ parallel with the x_3-axis, the net Burgers density vector, $\boldsymbol{B}$, lies within the x_1, x_2 plane.

4. Experimental results

In this section we report the results of the deformation of the grain boundary and lattice rotation measurements obtained from the EBSD measurements and results of the calculated GND densities associated with the lattice rotation measurements. We also report trajectories of the slip directions to consider the potential of dislocation transmission across the grain boundary.

4.1. Lattice rotations

The experimentally measured in-plane lattice rotation field is shown in Fig. 6 where a positive lattice rotation corresponds to counterclockwise rotation about the out-of-plane axis. The right and the left crystals are shown joined by the grain boundary indicated by the dashed line. It should be noted that the grain boundary was nominally straight prior to the introduction of plastic deformation. Thus the 'bowing out' of the grain boundary is due to the imposition of the plastic deformation.

As expected, the lattice rotation distribution in the region below the indenter in the right crystal follows the same general pattern reported previously for indentation into single FCC crystals of the same orientation (Dahlberg et al., 2014; Kysar et al., 2010). Directly beneath the indenter tip is a sharp jump in ω_3 where the lattice rotation transitions from about $+20^\circ$ to -20° across a distance of a few micrometers. This sharp jump is bordered on either side by narrow regions of large lattice

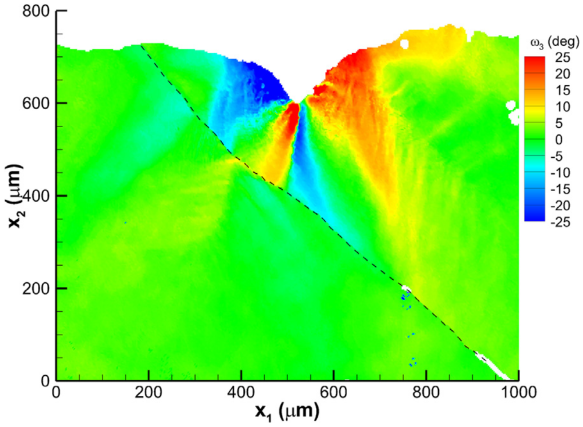

Fig. 6. Experimentally determined in-plane lattice rotation field ω_3. Dashed black line indicates position of grain boundary.

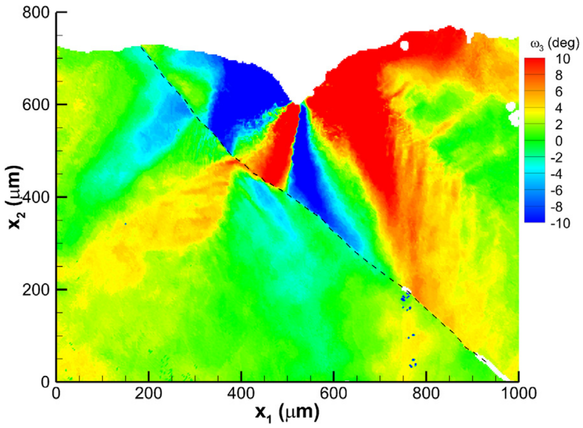

Fig. 7. Experimentally determined in-plane lattice rotation field ω_3 plotted with a narrow range of angles to show details in the left grain. Dashed black line indicates position of grain boundary.

rotations of opposite sign. In addition the two larger regions of high lattice rotation immediately beneath the surfaces at $\pm 45^\circ$ that had been in direct contact with the indenter surfaces are similar to the lattice rotation features reported previously. The magnitudes of lattice rotations in these regions depend upon the degree of plastic deformation as well as the degree of friction between the indenter and the indented surface.

The ω_3 features in the right crystal beneath the indenter tip and beneath the indented surfaces are—to first order—mirror images with respect to the vertical line passing through the indenter tip. However the grain boundary breaks the material mirror symmetry. Thus the lattice rotation distribution introduced by plastic deformation in the left crystal differs from that in the right crystal.

It is evident in Fig. 6 that the left crystal experienced significantly less lattice rotation than the right crystal. Thus the grain boundary served as an effective barrier against the transmission of plastic deformation. Interestingly, the portions of the left crystal with the largest lattice rotations abut against regions of the right crystal with the least lattice rotation. Such regions of low lattice rotation could be due to a small degree of plastic deformation but could also be due to simultaneous plastic slip on two (or more) slip systems whose respective lattice rotations are offsetting.

In Fig. 7 the lattice rotations have been plotted with a narrower range of magnitudes to further elucidate the state close to the grain boundary and in the left crystal. The magnitude of lattice rotations are significantly reduced to the left of the grain boundary such that ω_3 spans only $\pm 8^\circ$ right next to the grain boundary in the left crystal in contrast to a span of $\pm 12^\circ$ on the opposite side in the right crystal.

To plot the state in the immediate vicinity of the grain boundary we define a coordinate ζ that tracks the length of the grain boundary from the surface down into the specimen. In Fig. 8 the lattice rotations have been extracted on either side of the grain boundary and plotted against ζ. The data in each crystal corresponds to points along the boundary, but 3 μm into each grain from the boundary.

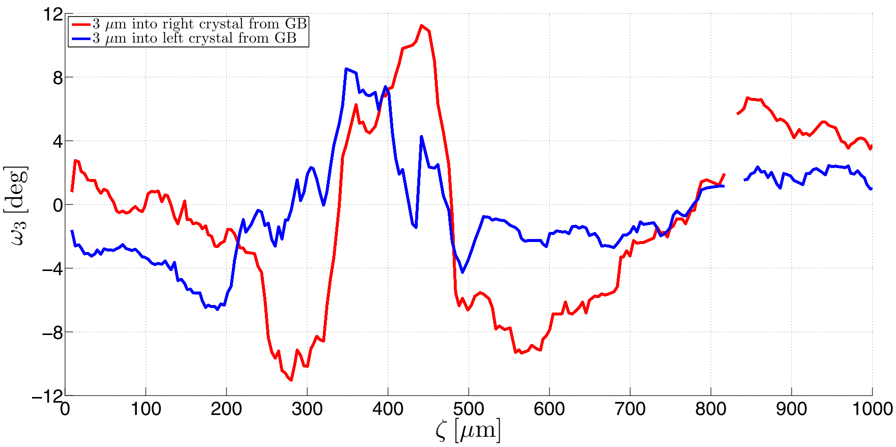

Fig. 8. Lattice rotation along lines tracking the grain boundary 3 μm on either side. Red and blue curves are extracted from the right and left crystal respectively (the same color scheme as in Fig. 3). The coordinate ζ follows the grain boundary from upper left to lower right. (For interpretation of the references to color in this figure legend, the reader is referred to the web version of this article.)

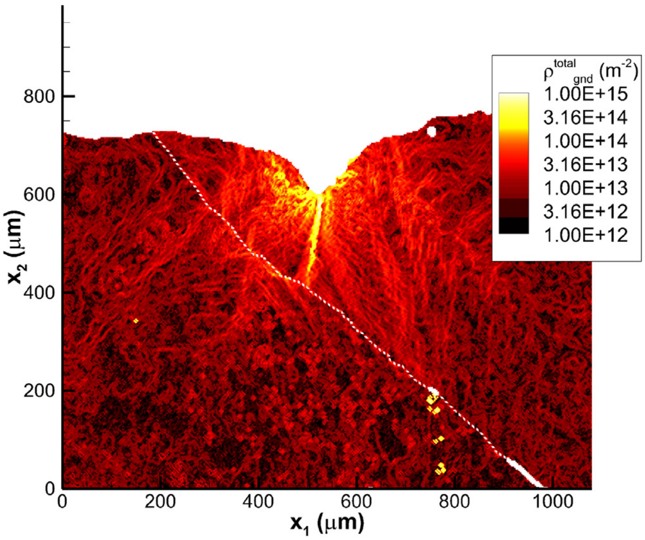

Fig. 9. Total geometrically necessary dislocation density $\rho^{\text{tot}}_{\text{gnd}}$.

4.2. Geometrically necessary dislocation densities

Spatially-resolved measurements of the lower bound on the total GND density, as defined in Eq. (6), are shown in Fig. 9. As will be discussed in Section 5.1, all three effective in-plane slip systems are expected to be active in only a small region of the deforming volume near the indented surface. Hence for all regions of interest in what follows, the lower bound solution corresponds to the actual solution.

The results of the total GND density in the right crystal are qualitatively similar to the results of total GND density measurements associated with wedge indentation into a nickel crystal of the same orientation in Kysar et al. (2010). The largest magnitude of GND densities approaches 10^{15} m^{-2} on the vertical line extending down from the indenter tip, which corresponds to the jump in lattice rotation. The measurements in the remaining parts of the crystal exhibit a quasiperiodic spacing consistent with the presence of dislocation substructures as observed via the characterization of GND densities in Landon et al. (2008), Wilkinson and Randman (2010), Öztop (2011), Sarac et al. (2016) and Field et al. (2012).

The measured GND densities are apportioned onto the three effective slip systems in Fig. 10 in both crystals. These results can be interpreted by noting the orientations of the three effective in-plane slip systems in both crystals in the undeformed reference configuration as well as the positive sense of the respective effective edge dislocations are indicated in Fig. 2b.

The GND measurements on individual effective slip systems within the right crystal are similar to the measurements reported in Kysar et al. (2010). A line of high GND densities extends down along the vertical line through the indenter tip.

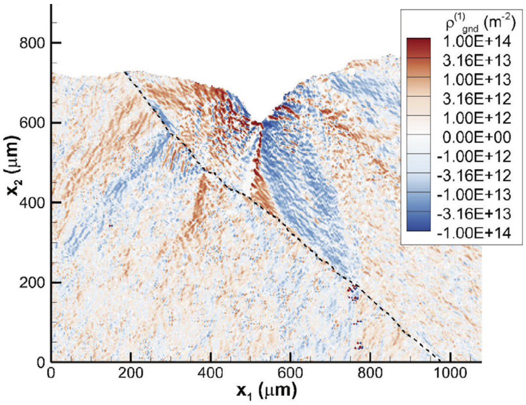

(a) $\rho^{(1)}_{\mathrm{gnd}}$

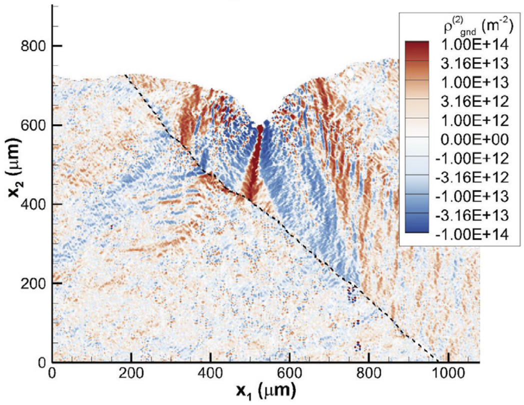

(b) $\rho^{(2)}_{\mathrm{gnd}}$

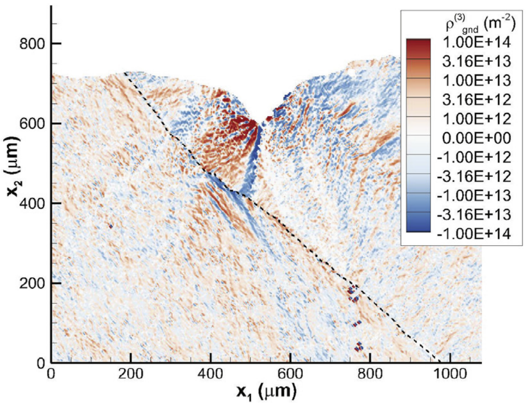

(c) $\rho^{(3)}_{\mathrm{gnd}}$

Fig. 10. Lower bound dislocation density map on the three effective slip systems in each crystal. Dashed black line indicates position of grain boundary.

Effective slip system 1 is responsible for the GND densities just to the right of the vertical line through the indenter tip and effective slip system 3 is responsible for the GND densities just to the left. This is consistent with the detailed single crystal plasticity analyses of Saito and Kysar (2011) and Saito et al. (2012). In addition, there is evidence that effective slip system 2 has been active in this region which can be explained as follows. The resolved shear stress on effective slip system 2 under the indenter tip must be zero initially due to symmetry; thus no slip should occur on that system at the earliest stages of deformation. Therefore slip activity evidently first took place on effective slip systems 1 and 3 until the lattice rotated to such an extent that the resolved shear stress on effective slip system 2 reached its critical stress after which

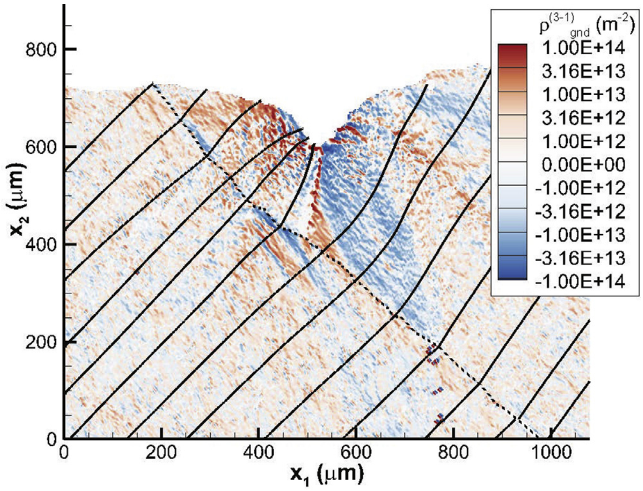

Fig. 11. Close alignment of the two co-planar slip systems across the grain boundary. Showing $\rho^{(3)}_{\rm gnd}$ in the left crystal and $\rho^{(1)}_{\rm gnd}$ in the right. Overlaid, represented by the black lines, are a continuous representation of the crystal plane orientation for effective slip planes $\boldsymbol{S}^{(3)}$ and $\boldsymbol{S}^{(1)}$, respectively.

it was activated and subsequently accumulated GND density. In addition to the general features of the GND densities, the quasi-periodic arrangement of the GND densities is more apparent for each of the effective slip systems. By comparing the apportionment of the GND densities on the three effective slip systems in Fig. 10 it is apparent that the overall magnitudes are approximately the same on each system with the exception of $\rho^{(2)}_{\rm gnd}$ (Fig. 10b) immediately under the indenter where the highest values exceed 10^{14} m^{-2}.

The spatial distribution of the GND densities changes dramatically across the grain boundary. Regions of high GND density in the left crystal are not as clearly defined and have a more diffuse character than in the right crystal. There are however still contiguous areas of same sense GND densities on each slip system. One example of this is immediately to the left of where the vertical line through the indenter tip meets the grain boundary at which point both $\rho^{(2)}_{\rm gnd}$ and $\rho^{(3)}_{\rm gnd}$ are concentrated in a small area abutting the grain boundary.

As discussed in Section 3, the orientation of $\boldsymbol{S}^{(3)}$ in the left crystal and $\boldsymbol{S}^{(1)}$ in the right crystal differ by 10.1023° prior to deformation. These effective in-plane slip systems are each comprised of a pair of coplanar dislocation slip systems. Thus this combination of slip systems has the potential to admit dislocation slip across the grain boundary with less resistance than any of the other possible combination of slip planes across the grain boundary in this specimen. (N.B. The angle between $\boldsymbol{S}^{(1)}$ in the left crystal and $-\boldsymbol{S}^{(3)}$ in the right crystal is 28.8401° so the transmission of slip across the grain boundaries with this combination of slip systems is expected to be more difficult. In addition effective slip system 2 consists of a collinear set of slip systems whereas effective slip systems 1 and 3 consist of coplanar sets of slip systems, so we do not expect plastic slip to transmit readily across the grain boundary between these slip systems.)

We now consider, in Fig. 11, the trajectories that are tangent to the local deformed values of $\boldsymbol{S}^{(3)}$ in the left crystal and of $\boldsymbol{S}^{(1)}$ in the right crystal. These lines corresponds physically to the as-deformed orientations of the respective slip systems in the two crystals. We refer to these trajectories as *crystallographic slip traces* because they are analogous to slip traces (e.g. Hirth and Lothe, 1982) that can be observed experimentally on the exterior surfaces of plastically deforming crystals. Prior to the introduction of plastic deformation, the crystallographic slip traces are straight lines within each grain that coincide with the orientations of the respective slip directions in Fig. 3b. After plastic deformation the crystallographic slip traces deform to reflect the as-deformed directions of $\boldsymbol{S}^{(3)}$ in the left crystal and of $\boldsymbol{S}^{(1)}$ in the right crystal.

In Fig. 11 the crystallographic slip traces have been overlaid on a GND density map of the same systems (i.e. $\rho^{(3)}_{\rm gnd}$ within the left crystal and $\rho^{(1)}_{\rm gnd}$ within the right crystal). Far away from the indenter tip (e.g. in the lower right) in regions that have undergone very little plastic deformation, the approximately 10° misalignment between $\boldsymbol{S}^{(3)}$ in the left crystal and of $\boldsymbol{S}^{(1)}$ at the grain boundary is evident due to the abrupt kink in the crystallographic slip trace across the grain boundary. However, upon examining the region close to the grain boundary under the indenter tip it can be seen that there is significantly less misalignment between $\boldsymbol{S}^{(3)}$ in the left crystal and of $\boldsymbol{S}^{(1)}$ across the grain boundary. Furthermore in this region, the right crystal has higher GND density than the left crystal has immediately across the grain boundary. This suggests that plastic deformation with slip direction $\boldsymbol{S}^{(1)}$ in the right crystal led to lattice rotation that caused the local direction of $\boldsymbol{S}^{(1)}$ at the grain boundary to rotate into alignment with $\boldsymbol{S}^{(3)}$ in the left crystal. Evidence of similar behavior have been reported by Zaeffer et al. (2003) in channel-die compression experiments of Al bicrystals.

The two slip systems that cooperatively combine to form coplanar effective slip systems 1 and 3 have crystallographic Burgers vectors with directions 30° in and out of the plane of deformation. Thus the actual slip systems that induce the in-plane plastic deformation contain dislocation loops in which various regions have edge, screw and mixed character. Experiments by Davis et al. (1966) and Lim and Raj (1985) in FCC bicrystals showed that screw components of dislocations pass though a tilt grain boundary (i.e. $\boldsymbol{l}_{\text{in}} = \boldsymbol{l}_{\text{out}}$) unimpeded if the Burgers vector of the incoming slip plane is parallel to the grain boundary (i.e. $\boldsymbol{b}_{\text{in}} = \boldsymbol{b}_{\text{out}}$ is parallel to $\boldsymbol{l}_{\text{in}} = \boldsymbol{l}_{\text{out}}$) such that $\boldsymbol{b}_{\text{r}} = \boldsymbol{0}$. The screw components of the dislocations in the coplanar effective slip systems do not satisfy this condition. As a consequence, both screw and edge components of the incoming dislocations are expected to be impeded as they arrive at the grain boundary. In addition, the effective slip systems 1 and 3 are comprised of coplanar pairs of slip systems. The unit normal vectors to both coplanar pairs themselves lie in a plane, which implies that the intersections of effective slip systems 1 and 3 at the grain boundary consist of lines rather than points. As a consequence, dislocation lines can, in principle, transmit across the grain boundary between these two sets of effective coplanar slip systems. Therefore any transmission of plastic slip across the grain boundary will occur due to the second transmission mechanism discussed in Section 2, which leaves a non-zero $\boldsymbol{b}_{\text{r}}$ in the grain boundary and offers intermediate resistance to the transmission of plastic slip relative to the other two mechanisms.

The dislocation transmission impediment due to the relative orientations of the slip systems and the grain boundary accounts for the buildup of $\rho^{(1)}_{\text{gnd}}$ to the right side of the grain boundary near $x_1 = 600$ µm and $x_2 = 300$ µm in Fig. 11 compared to the smaller $\rho^{(3)}_{\text{gnd}}$ to the left of the grain boundary, reminiscent of what Sun et al. (2000) observed.

This result suggests that plastic deformation in the right crystal introduced a negative lattice rotation that brought $\boldsymbol{S}^{(1)}$ in the right crystal into alignment of $\boldsymbol{S}^{(3)}$ in the left crystal where much less plastic deformation occurred. It is significant that the lattice rotation at the grain boundary in the right crystal did not 'overshoot' the orientation in the left crystal. This suggests that as $\boldsymbol{S}^{(1)}$ in the right crystal came into alignment with $\boldsymbol{S}^{(3)}$ in the left crystal that dislocation motion subsequently occurred with minimal impediment across the grain boundary and the two slip systems subsequently rotated in tandem at the grain boundary.

5. Finite element method simulation

The experiment was modeled with the finite element method (FEM) using an elastically and plastically anisotropic crystal plasticity constitutive description implemented as a UMAT user material subroutine (Huang, 1991; Kysar, 1997) in the commercially available software ABAQUS. Cubic anisotropy was defined via the elasticity coefficients $C_{11} = 108.2$ GPa, $C_{12} = 61.3$ GPa and $C_{44} = 28.5$ GPa for aluminum given in Hirth and Lothe (1982). The inelastic behavior was modeled by a viscous single crystal plasticity formulation using the constitutive relations by Peirce et al. (1982, 1983). The initial and saturation stress on each slip plane was set to $\tau_0 = 20$ MPa and $\tau_s = 100$ MPa respectively and the initial hardening slope was $h_0 = 200$ MPa. The viscous power law exponent was set to $n = 60$ and the reference slip rate was $\dot{\gamma}_0 = 0.001$ s^{-1}. Latent hardening was assumed equal to the self hardening by setting the parameter $q = 1$. A finite deformation formulation was used to simulate the experiment.

The model used two-dimensional plane strain 4-node quadrilateral elements, except at the grain boundary where triangular elements were used. Overall 34,728 quadrangle elements and 394 triangular elements were employed in a mesh that was made progressively coarser further away from the indent and grain boundary. The elements on either side of the grain boundary shared nodes along it so that no relative movement occurred along the boundary. No explicit grain boundary constitutive model was used and the influence of the grain boundary appeared only due to the difference of crystallographic orientation on either side.

The tungsten carbide (WC) indenter was modeled as rigid since WC is about an order of magnitude stiffer than Al. Frictional contact was defined between the analytical surface of the indenter and the top boundary of the bicrystal with a frictional coefficient $\mu = 0.5$. This value likely overestimates the frictional effects but was deemed acceptable since it only influences a small region of the solution close to the contact and it significantly improved the convergence rate. The indenter tip radius was given a larger value than in the experiments so that a larger element size could be used to avoid large stress concentrations initially before a larger region of indenter/material have come into contact. This will influence the solution close to the indenter tip and the region just below it.

Boundary conditions (fixed) were applied sufficiently far away from the indenter to have negligible influence on the solution (this assumption was checked *a posteriori* by confirming that stress and strain fields tended to zero outside the region of interest). The loading was applied by prescribing that the indenter impinge into the crystal at a constant downwards velocity such that quasistatic conditions were maintained throughout the whole load history. The solution was carried out over more than 50,000 load increments using the generalized mid-point method without iterations in the increments. To avoid a problem with zero-energy hour-glass deformation modes in a region of high hydrostatic stress below the indenter a small amount (approx $\frac{1}{54}$ of C_{11}) of artificial hour-glass stiffness was introduced and selectively reduced integration elements were used.

5.1. Results and comparison to experiments

The spatial distribution of lattice rotation, ω_3, from the FEM solution is shown in Fig. 12 compared to the experimental results from Fig. 6. The simulations capture all the major features of the lattice rotation field, at least qualitatively. The narrow region below the tip where a large difference in ω_3 forms the 'jump' discontinuity is similar to the corresponding region in Fig. 6. Quantitative discrepancies in this region of the FEM solution are that the region of high rotation is narrower,

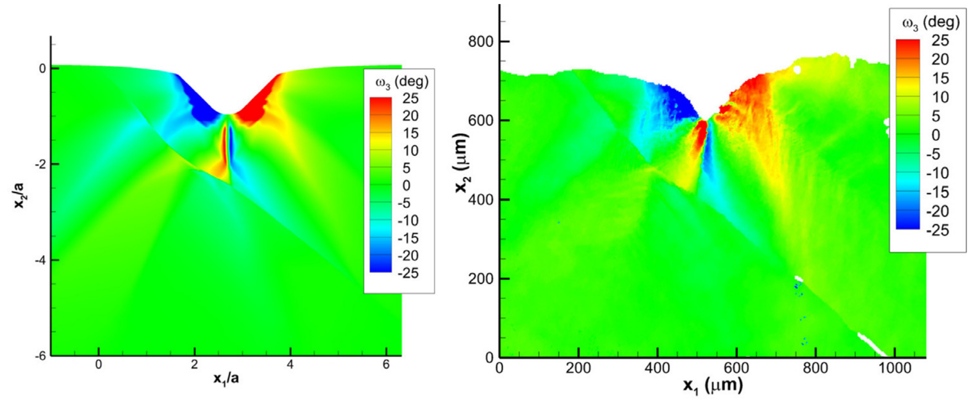

Fig. 12. Comparison of the ω_3-field from FEM (left) and from the experiment.

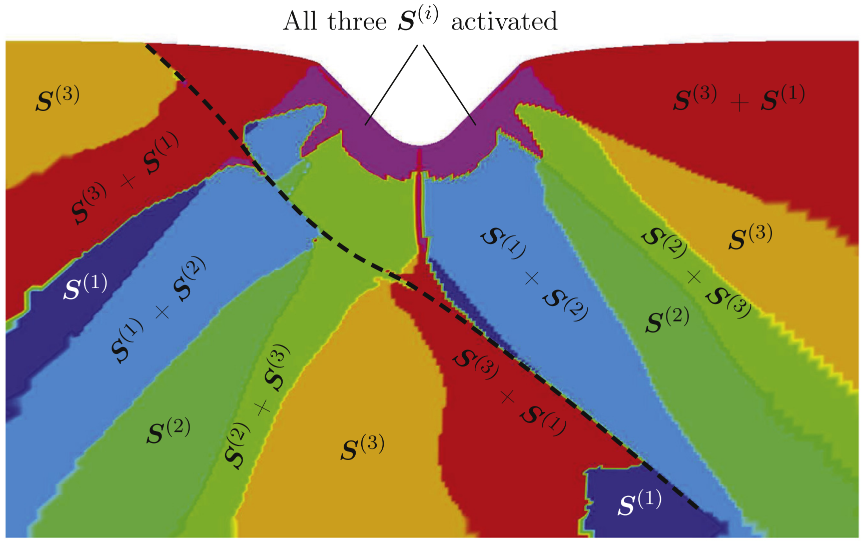

Fig. 13. Slip system activity map where colored regions corresponds to regions within the crystal with predominant slip on the systems indicated in the annotations. Only a small region close to the indenter slips on all three in-plane effective slip systems.

it does not extend to the upper surface and it extends further down where the lower termination has angled extensions away from the vertical line through the indenter tip. There is evidence of these extensions in the experiment but they are much less pronounced. There also is a less sharp transition visible where a thin strip along the vertical line with $\omega_3 \approx 0$ in the simulation prevents the two regions of opposite sign from forming a sharp jump—this is however only a consequence of the FEM interpolation and the Gauss point values show the same dramatic transition as the experiment.

The two large regions extending into the crystal from the $\pm$ 45° flanks of the indenter appear overall similar to the experiments, but the details of the shapes differ. The ‘arms’ extending down in the crystal are not as inclined from the surface and their extensions into the crystal in the simulations are more diffuse than in the experiments.

The maximum magnitude of ω_3 is about 40° in the contact zone, which is larger than the experimental measurements. This is probably due to the high coefficient of friction influencing the solution locally in that region, but there is also a tendency to overestimate (by a few degrees) the lattice rotations on either side of line below the indenter.

The ‘bowing out’ of the grain boundary is present in almost identical shape in both experiment and FE-solution. The pattern of ω_3 in the right crystal is again similar to the experiment but is slightly overestimated in terms of magnitude.

One characteristic of plasticity in single crystals is that plastic slip typically occurs on well-defined sets of slip systems in contiguous regions of the deforming domain (e.g. Rice, 1973, 1987; Kysar et al., 2005). We refer to these regions as *plastic slip sectors*. Fig. 13 shows the predicted plastic slip sectors of the plastically deformed bicrystal calculated by post-processing of the FEM solution as described in Dahlberg et al. (2014). It is apparent that only one or two effective plastic slip systems are active in the vast majority of the plastic zone surrounding the indented region. Thus we expect the experimentally-determined GND densities in such regions to represent the actual GND density values, as discussed in relation to the lower

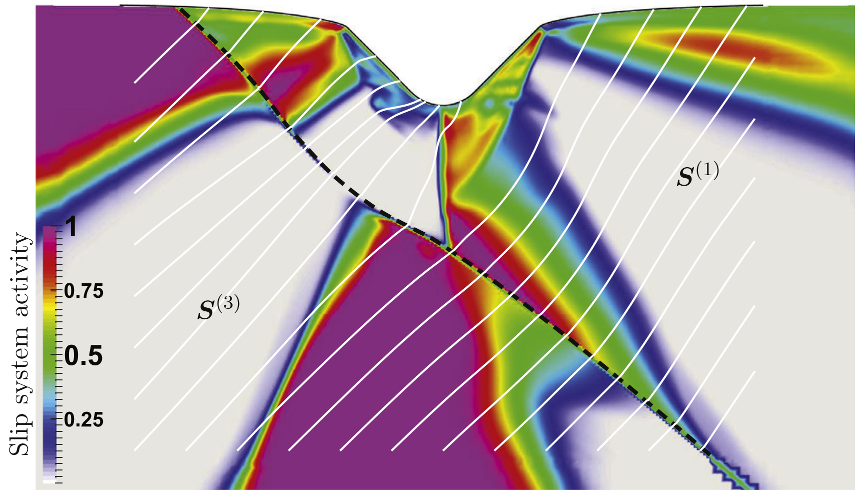

Fig. 14. Level of accumulated slip (in relation to total slip in each point) on the two slip systems that nearly line up across the grain boundary, $\boldsymbol{S}^{(3)}$ to the left and $\boldsymbol{S}^{(1)}$ to the right. Overlaid, represented by the white lines, are a continuous representation of the crystal plane orientation for effective slip planes $\boldsymbol{S}^{(3)}$ and $\boldsymbol{S}^{(1)}$, respectively. The deformed position of the grain boundary is indicated by the dashed black line.

bound solutions of ρ_{gnd}^{tot} in Eq. (6). The simulation predicts that all three slip systems have contributed to plastic deformation only in a small region very near the indenter tip due to the very large lattice rotations and finite deformations that result in a highly non-proportional loading on these material points. Hence the GND densities measured in regions immediately surrounding the indenter tip should be considered to be only the lower bound on the total GND density.

Fig. 13 predicts a plastic slip sector in the right crystal where slip on $\boldsymbol{S}^{(1)}$ contributed all or some of the plastic deformation. Immediately across the grain boundary is a region of the left crystal where slip on $\boldsymbol{S}^{(3)}$ contributed all or some of the plastic deformation. As shown in Fig. 11, it is in this region where plastic deformation in the right crystal led to lattice rotation that brought $\boldsymbol{S}^{(1)}$ in the right crystal into alignment with $\boldsymbol{S}^{(3)}$ in the left crystal. Hence the predicted active slip systems from the FEM analysis, as shown in Fig. 14, are consistent with the experimental observations.

6. Discussion

There is evidence of a dislocation pile-up at the grain boundary in Fig. 9 that induced significant lattice rotation in the right crystal. The dislocation density at the grain boundary at coordinates $x_1 = x_2 \approx 450\,\mu\text{m}$ is locally about an order of magnitude larger than in the surrounding material. This region of positive lattice rotation—emanating down from the indenter tip—abruptly terminates against the grain boundary. There is no evidence that any significant lattice rotation features are transmitted across the grain boundary and one can therefore conclude that it is the kinematics and interactions of dislocations within crystals and within grain boundaries that dominate the behavior and not an imposed deformation gradient field by the wedge indenter.

As discussed in Section 5, no constitutive behavior is ascribed to the grain boundary in the FEM simulation. Hence the simulated grain boundary affects the deformation state only via jumps in slip system resolved shear stress. From a dislocation mechanics perspective, such a grain boundary does not impede the transmission of a dislocation because there is no energetic cost due to formation of a residual dislocation. Therefore with regard to Fig. 11, after $\boldsymbol{S}^{(1)}$ in the right crystal rotates into alignment with $\boldsymbol{S}^{(3)}$ in the left crystal, subsequent plastic deformation in that region occurs as if the grain boundary did not exist.

The classical local constitutive hardening model employed in this study does not account for plastic strain gradients or the presence of an intrinsic length scale of crystal plasticity. However given the length scale pertinent to the experimental resolution, i.e. $3\,\mu\text{m}$, the absence of an explicit grain boundary model and the use of a local theory of crystal plasticity does not influence the simulation results in comparison to the experiments to any large extent. This may at first seem to be at odds with the recent effort of understanding and modeling plastic deformation as a strongly length scale dependent phenomena. However, in terms of higher order strain gradient plasticity theories (e.g. Gudmundson, 2004) where grain boundaries can be introduced explicitly as internal constraints to unimpeded plastic flow (see for instance van Beers et al., 2015a; 2015b; Dahlberg et al., 2013) the local effect from one single such constraint will only influence a region on the order of the constitutive plastic length scale. Since this length scale is usually thought to be on the order of $1\,\mu\text{m}$ or less the effects here would be difficult to resolve experimentally. On the other hand, if the length scale is thought to correlate to a dislocation mean free path in the crystal (e.g. Kysar et al., 2010; Öztop, 2011) then the high purity crystals used here will initially have a larger length scale than usually quoted for typical engineering materials and a non-local plasticity model could possibly be able to better capture the details of the experiments in the region with a large inhomogeneity in plastic slip.

Finally, the constitutive model assumes Taylor hardening ($q = 1$) between active and latent slip systems. This is an approximation to the real relationship between hardening on different slip planes and may be a source of discrepancy between the simulations and experiments.

7. Conclusions and outlook

We report herein the results of experiments to characterize the lattice rotation and the GND density distributions in an aluminum bicrystal with a symmetric tilt grain boundary. The following conclusions can be drawn from the study.

- An aluminum bicrystal with a symmetric tilt grain boundary was indented with a wedge to induce a plane strain state of plastic deformation that straddled the grain boundary.
- Spatially resolved lattice rotation measurements in the deformed configuration demonstrate significant “bowing” of the initially nominally straight grain boundary.
- The grain boundary served as a significant impediment to the transmission of plastic slip along much of its length.
- Dislocation transmission across the grain boundary occurred between two active coplanar pairs of effective in-plane (i.e. plane strain) slip systems with an initial misorientation of 10.1023°, leaving dislocations with a residual Burgers vector in the grain boundary.
- Plastic deformation on the active coplanar slip systems in the more highly deformed crystal caused its slip plane to rotate into alignment with the slip plane of the coplanar slip systems in the adjoining crystal.
- Subsequently, the two coplanar pairs of slip systems rotated in tandem, suggesting a significant diminution of the impediment to dislocation transmission across the grain boundary.
- A detailed single crystal plasticity simulation of the experiment based upon a local constitutive hardening model captures the general features of the experiments.

Future experimental studies of this type should employ High Resolution EBSD to make spatially resolved lattice rotation measurements with a significantly smaller experimental uncertainty (e.g. Gardner et al., 2011). In this way the jump in GND density content as well as the jump in net Burgers density vector can be measured across the grain boundary with greater fidelity, which should afford even deeper insight into the transmission of plastic slip across a grain boundary.

Future crystal plasticity models should include constitutive behavior of the grain boundary to account for the barrier to dislocation transmission across a grain boundary that exists due to the atomic complexity of the grain boundary. In addition, the single crystal constitutive behavior in future studies should account for the evolution of dislocation densities and the associated characteristic length scales of crystal plasticity. For a compelling argument that this is the case see the recent work by Reuber et al. (2014) where a nonlocal crystal plasticity theory is used to obtain a very good agreement to the experimental data in Kysar et al. (2010) and Dahlberg et al. (2014). In addition, due to the very large deformations and mesh distortion directly under the indenter, future studies should employ remeshing methods to increase accuracy and reduce the possibility of mesh dependence.

Acknowledgments

C.F.O. Dahlberg gratefully acknowledges support from The Sweden-America Foundation Fellowship and Vetenskapsrådet (VR E0566901). J.W. Kysar gratefully acknowledges support from the National Science Foundation (DMR-1310503).

Appendix A. Specimen crystallographic arrangement

An aluminum bicrystal with a $\Sigma 43\,(3\,3\,5)[1\,1\,0]$ symmetric tilt coincident site lattice (CSL) grain boundary is considered. We discuss the methodology used to grow a bicrystal of the desired orientations, from which the test specimen is excised. First consider an as-grown and fully annealed FCC single crystal aligned as shown in Fig. 15.

The angle between the $\left[1\,\bar{1}\,0\right]$ direction and the $\left[5\,\bar{5}\,6\right]$ direction is $\alpha = \cos^{-1}(5/\sqrt{43}) \approx 40.3155°$, so that $\beta \approx 49.6845°$. The grain boundary is a high angle grain boundary with a tilt angle of 2α. A direction that is fixed in the sample coordinate system and that is parallel with a $\langle 1\,1\,0\rangle$-direction in one grain will in the other crystal be of the $\langle 1\,1\,a\rangle$-type. The angle from $[1\,1\,a]$ to $[0\,0\,1]$ should be $\theta = \pi/2 - 2\alpha$, from which a can be determined exactly

$$\cos\theta = \frac{a}{\sqrt{2+a^2}} \quad \Rightarrow \quad a = \sqrt{\frac{2\cos^2\theta}{1-\cos^2\theta}} = \frac{60}{7}. \tag{8}$$

The method used to create the bicrystal is outlined in Fig. 16. First the crystal is split into two pieces along the $\left[\bar{3}\,3\,5\right]$ direction forming pieces **A** and **B**, as indicated in Fig. 16a. Piece **B** is then rotated 180° as indicated in Fig. 16b, the parts are combined again and the bicrystal is grown from which a test specimen is cut out (see Fig. 16c). The resulting test specimen is shown in Fig. 16d.

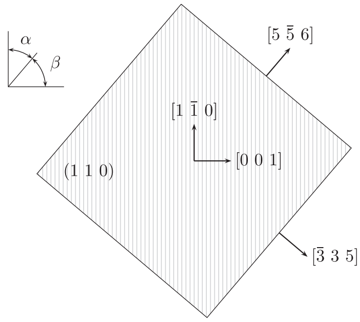

Fig. 15. Original crystal with crystallographic directions indicated. The thin lines indicate effective slip system 2, where positive slip is in the direction of $[1\,\bar{1}\,0]$.

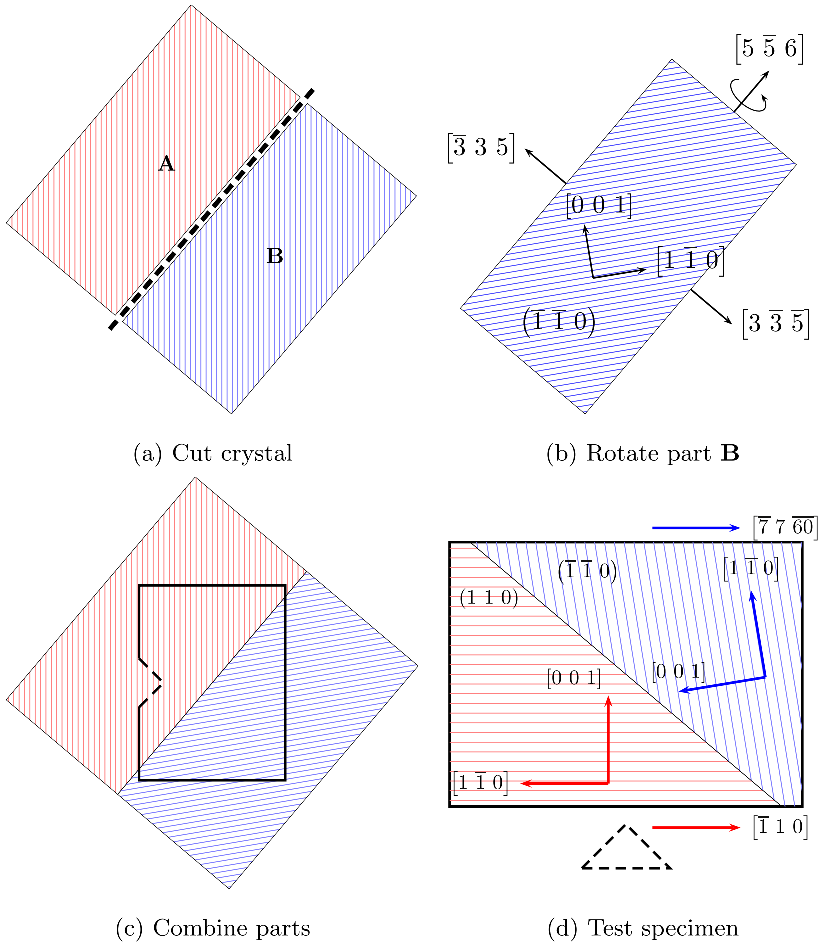

Fig. 16. Illustrations mimicking the procedure to create the bicrystal. (a) Cut separating crystal in Fig. 15 into two pieces. (b) Flipping over one of the parts. (c) After bicrystal growth, excise test specimen. (d) Test specimen with crystallographic direction indicated.

References

Abuzaid, W.Z., Sangid, M.D., Carroll, J.D., Sehitoglu, H., Lambros, J., 2012. Slip transfer and plastic strain accumulation across grain boundaries in Hastelloy X. J. Mech. Phys. Solids 60 (6), 1201–1220.

Arsenlis, A., Parks, D., 1999. Crystallographic aspects of geometrically necessary and statistically-stored dislocation density. Acta Materialia 47 (5), 1597–1611.

Aust, K.T., Chen, N.K., 1954. Effect of orientation difference on the plastic deformation of aluminum bicrystals. Acta Metallurgica 2 (4), 632–638.

Bayerschen, E., McBride, A.T., Reddy, B.D., Böhlke, T., 2016. Review on slip transmission criteria in experiments and crystal plasticity models. J. Mater. Sci. 51 (5), 2243–2258.

van Beers, P., Koutznetsova, V., Geers, M., 2015a. Grain boundary interfacial plasticity with incorporation of internal structure and energy. Mech. Mater. 90, 69–82.
van Beers, P., Koutznetsova, V., Geers, M., Tschopp, M., McDowell, D., 2015b. A multiscale model of grain boundary structure and energy: from atomistics to a continuum description. Acta Materialia 82, 513–529.
Bieler, T.R., Eisenlohr, P., Zhang, C., Phukan, H.J., Crimp, M.A., 2014. Grain boundaries and interfaces in slip transfer. Current Opinion Solid State Mater. Sci. 18 (4), 212–226.
Bollmann, W., 1970. Crystal Defects and Crystalline Interfaces. Springer-Verlag, Berlin Heidelberg.
Bragg, W.L., 1940. Discussion. Part I. Proc. Phys. Soc. 52 (1), 54–57.
Burgers, J.M., 1939. Some considerations on the fields of stress connected with dislocations in a regular crystal lattice. I.. In: Proceedings of the Section of Sciences / Koninklijke Nederlansche Akademie van Wetenschappen., 42, pp. 293–325.
Clark, R., Chalmers, B., 1954. Mechanical deformation of aluminium bicrystals. Acta Metallurgica 2 (1), 80–86.
Clark, W.A.T., Wagoner, R.H., Shen, Z.Y., Lee, T.C., Robertson, I.M., Birnbaum, H.K., 1992. On the criteria for slip transmission across interfaces in polycrystals. Scripta Metallurgica et Materialia 26 (2), 203–206.
Dahlberg, C., Saito, Y., Öztop, M., Kysar, J.W., 2014. Geometrically necessary dislocation density measurments associated with different angles of indentations. Int. J. Plastic. 54, 81–95.
Dahlberg, C.F.O., Faleskog, J., Niordson, C.F., Legarth, B.N., 2013. A deformation mechanism map for polycrystals modeled using strain gradient plasticity and interfaces that slide and separate. Int. J. Plastic. 54, 81–95.
Davis, K.G., Teghtsoonian, E., Lu, A., 1966. Slip band continuity across grain boundaries in aluminum. Acta Metallurgica 14 (12), 1677–1684.
Eshelby, J.D., Frank, F.C., Nabarro, F.R.N., 1951. The equilibrium of linear arrays of dislocations. Philosoph. Mag. 42 (327), 351–364.
Field, D.P., Merriman, C.C., Allain-Bonasso, N., Wagner, F., 2012. Quantification of dislocation structure heterogeneity in deformed polycrystals by EBSD. Modell. Simul. Mater. Sci. Eng. 20 (2), 024007.
Frank, F.C., 1951. Crystal dislocations–elementary concepts and definitions. Philosoph. Mag. 42 (331), 809–819.
Gan, Y.X., Kysar, J.W., 2007. Cylindrical void in a rigid-ideally plastic single crystal III: hexagonal close-packed crystal. Int. J. Plastic. 23 (4), 592–619.
Gan, Y.X., Kysar, J.W., Morse, T.L., 2006. Cylindrical void in a rigid-ideally plastic single crystal II: experiments and simulations. Int. J. Plastic. 22, 39–72.
Gardner, C.J., Kacher, J., Basinger, J., Adams, B.L., Öztop, M.S., Kysar, J.W., 2011. Techniques and applications of the simulated pattern adaptation of Wilkinson's method for advanced microstructure analysis. Exp. Mech. 51 (8), 1379–1393.
Gudmundson, P., 2004. A unified treatment of strain gradient plasticity. J. Mech. Phys. Solids 52, 1379–1406.
Gupta, V., Agnew, S., 2010. A simple algorithm to eliminate ambiguities in ebsd orientation map visualization and analyses: application to fatigue crack--tips/wakes in aluminum alloys. Microsc. Microanal. 16, 831–841.
Hall, E.O., 1951. The deformation and ageing of mild steel: III discussion of results. Proc. Phys. Soc. 64 (9), 747–753.
Hirth, J., Lothe, J., 1982. Theory of Dislocations. John Wiley and Sons, New York.
Huang, Y., 1991. A user-material subroutine incorporating single crystal plasticity in the ABAQUS finite element program, Mech Report 178. Technical Report. Division of Engineering and Applied Sciences, Harvard University, Cambridge, MA.
Kacher, J., Eftink, B.P., Cui, B., Robertson, I.M., 2014. Dislocation interactions with grain boundaries. Current Opinion Solid State Mater. Sci. 18 (4), 227–243.
Kysar, J.W., 1997. Addendum to "A user-material subroutine incorporating single crystal plasticity in the ABAQUS finite element program, Mech Report 178. Technical Report. Division of Engineering and Applied Sciences, Harvard University, Cambridge, MA.
Kysar, J.W., 2000. Directional dependence of fracture in copper/sapphire bicrystal. Acta Materialia 48 (13), 3509–3524.
Kysar, J.W., 2001a. Continuum simulations of directional dependence of crack growth along a copper/sapphire bicrystal interface. Part I: experiments and crystal plasticity background. J. Mech. Phys. Solids 49 (5), 1099–1128.
Kysar, J.W., 2001b. Continuum simulations of directional dependence of crack growth along a copper/sapphire bicrystal interface. Part II: crack tip stress/deformation analysis. J. Mech. Phys. Solids 49 (5), 1129–1153.
Kysar, J.W., Briant, C.L., 2002. Crack tip deformation fields in ductile single crystals. Acta Materialia 50 (9), 2367–2380.
Kysar, J.W., Gan, Y.X., Mendez-Arzuza, G., 2005. Cylindrical void in a rigid-ideally plastic single crystal I: anisotropic slip line theory solution for face-centered cubic crystals. Int. J. Plastic. 21, 1481–1520.
Kysar, J.W., Gan, Y.X., Morse, T.L., Chen, X., Jones, M.E., 2007. High strain gradient plasticity associated with wedge indentation into face-centered cubic single crystals: geometrically necessary dislocation densities. J. Mech. Phys. Solids 55 (7), 1554–1573.
Kysar, J.W., Saito, Y., Öztop, M., Lee, D., Huh, W., 2010. Experimental lower bounds on geometrically necessary dislocation density. Int. J. Plastic. 26 (8), 1097–1123.
Landon, C.D., Adams, B.L., Kacher, J., 2008. High-resolution methods for characterizing mesoscale dislocation structures. J. Eng. Mater. Technol.-Trans. Asme 130 (2), 21004.
Larson, B.C., Yang, W., Tischler, J.Z., Ice, G.E., Budai, J.D., Liu, W., Weiland, H., 2004. Micron-resolution 3-D measurement of local orientations near a grain-boundary in plane-strained aluminum using X-ray microbeams. Int. J. Plastic. 20 (3), 543–560.
Lee, T.C., Robertson, I.M., Birnbaum, H.K., 1989. Prediction of slip transfer mechanisms across grain boundaries. Scripta Metallurgica 23 (5), 799–803.
Lee, T.C., Robertson, I.M., Birnbaum, H.K., 1990. TEM In situ deformation study of the interaction of lattice dislocations with grain boundaries in metals. Philosoph. Mag. A 62 (1), 131–153.
Lim, L.C., Raj, R., 1985. Continuity of slip screw and mixed crystal dislocations across bicrystals of nickel at 573 k. Acta Metallurgica 33 (8), 1577–1583.
Livingston, J.D., Chalmers, B., 1957. Multiple slip in bicrystal deformation. Acta Metallurgica 5 (6), 322–327.
Marcinkowski, M.J., Tseng, W.F., 1970. Dislocation behavior at tilt boundaries of infinite extent. Metallurg. Trans. 1 (12), 3397–3401.
McDowell, D.L., 2010. A perspective on trends in multiscale plasticity. Int. J. Plastic. 26 (9), 1280–1309.
Mercier, D., Zambaldi, C., Bieler, T. R., 2016. Slip transfer analysis toolbox.
Miura, S., Saeki, Y., 1978. Plastic deformation of aluminum bicrystals <100> oriented. Acta Metallurgica 26, 93–101.
Nye, J.F., 1953. Some geometrical relations in dislocation solids. Acta Metallurgica 1, 153–162.
Ohashi, T., Barabash, R.I., Pang, J.W.L., Ice, G.E., Barabash, O.M., 2009. X-Ray microdiffraction and strain gradient crystal plasticity studies of geometrically necessary dislocations near a ni bicrystal grain boundary. Int. J. Plastic. 25 (5), 920–941.
Okada, T., Kotaka, M., Wada, T., Tagami, M., Inoko, F., 2006. Deformation and recrystallization of aluminum bicrystals having asymmetric tilt grain boundary. Mater. Trans. 47 (3), 838–844.
Öztop, M., 2011. Multiscale Experimental Analysis in Plasticity: Linking Dislocation Structures to Continuum Fields. Columbia University Ph.D. thesis.
Peirce, D., Asaro, R., Needleman, A., 1982. An analysis of nonuniform and localized deformation in ductile singel crystals. Acta Metallurgica 30, 1087–1119.
Peirce, D., Asaro, R., Needleman, A., 1983. Material rate dependence and localized deformation in crystalline solids. Acta Metallurgica 31 (12), 1951–1976.
Petch, N.J., 1953. The cleavage strength of polycrystals. J. Iron and Steel Inst. 174, 25–28.
Read, W.T., Shockley, W., 1950. Dislocation models of crystal grain boundaries. Phys. Rev. 78 (3), 275–289.
Reid, C.N., Owen, W.S., 1973. Deformation Geometry for Materials Scientists. Pergamon, Oxford.
Reuber, C., Eisenlohr, P., Roters, F., Raabe, D., 2014. Dislocation density distribution around an indent in single-crystalline nickel: comparing nonlocal crystal plasticity finite-element predictions with experiments. Acta Materialia 71 (1), 333–348.
Rey, C., Zaoui, A., 1980. Slip heterogeneities in deformed aluminium bicrystals. Acta Metallurgica 28, 687–697.
Rice, J.R., 1968. Mathematical analysis in the mechanics of fracture. In: Liebowitz, H. (Ed.), Fracture: An Advanced Treatise, 2,. Academic Press, New York, chapter 3, pp. 191–311.
Rice, J.R., 1973. Plane strain slip line theory for anisotropic rigid/plastic materials. J. Mech. Phys. Solids 21 (2), 63–74.
Rice, J.R., 1987. Tensile crack tip fields in elastic ideally plastic crystals. Mech. Mater. 6 (4), 317–335.

Saito, Y., Kysar, J.W., 2011. Wedge indentation into elastic–plastic single crystals, 1: asymptotic fields for nearly-flat wedge. Int. J. Plastic. 27 (10), 6374–6381.
Saito, Y., Öztop, M., Kysar, J.W., 2012. Wedge indentation into elastic–plastic single crystals, 2: simulations for face-centered cubic crystals. Int. J. Plastic. 28 (1), 70–87.
Sarac, A., Oztop, M.S., Dahlberg, C.F.O., Kysar, J.W., 2016. Spatial distribution of the net burgers vector density in a deformed single crystal. Int. J. Plastic. 85, 110–129.
Shen, Z., Wagoner, R.H., Clark, W.A.T., 1986. Dislocation pile-up and grain boundary interactions in 304 stainless steel. Scripta Metallurgica 20 (6), 921–926.
Shen, Z., Wagoner, R.H., Clark, W.A.T., 1988. Dislocation and grain boundary interactions in metals. Acta Metallurgica 36 (12), 3231–3242.
Smith, L., Farkas, D., 2016. Non-planar grain boundary structures in fcc metals and their role in nano-scale deformation mechanisms. Philosoph. Mag. 94 (2), 152–173.
Soer, W.A., De Hosson, J.T.M., 2005. Detection of grain-boundary resistance to slip transfer using nanoindentation. Mater. Lett. 59 (24–25), 3192–3195.
Spearot, D.E., Sangid, M.D., 2014. Insights on slip transmission at grain boundaries from atomistic simulations. Current Opinion Solid State Mater. Sci. 18 (4), 188–195.
Sun, S., Adams, B.L., King, W.E., 2000. Observations of lattice curvature near the interface of a deformed aluminium bicrystal. Philosoph. Mag. a-Phys. Condensed Matter Struct. Defects Mech. Properties 80 (1), 9–25.
Sutton, A.P., Balluffi, R.W., 1995. Interfaces in Crystalline Materials. Clarendon Press, Oxford.
Taylor, G.I., 1934. The mechanism of plastic deformation of crystals. Part I. Theoretical. Proc. R. Soc. London. Series A 145 (855), 362–387.
Tschopp, M.A., Coleman, S.P., Mcdowell, D.L., 2015. Symmetric and asymmetric tilt grain boundary structure and energy in cu and al (and transferability to other fcc metals). Integrating Mater. Manuf. Innov. 4 (11), 1–14.
Tschopp, M.A., McDowell, D.L., 2007. Structures and energies of Σ 3 asymmetric tilt grain boundaries in copper and aluminium. Philosoph. Mag. 87 (22), 3147–3173.
Tsuru, T., Shibutani, Y., Hirouchi, T., 2016. A predictive model for transferability of plastic deformation through grain boundaries. AIP Adv. 6 (015004), 1–9.
Vachhani, S., Doherty, R., Kalidindi, S., 2016. Studies of grain boundary regions in deformed polycrystalline aluminum using spherical nanoindentation. Int. J. Plastic. 81, 87–101.
Van Swygenhoven, H., Farkas, D., Caro, A., 2000. Grain-boundary structures in polycrystalline metals at the nanoscale. Phys. Rev. B 62 (2), 831–838.
Van Swygenhoven, H., Weertman, J.R., 2006. Deformation in nanocrystalline metals. Mater. Today 9 (5), 24–31.
Wang, M.G., Ngan, A.H.W., 2004. Indentation strain burst phenomenon induced by grain boundaries in niobium. J. Mater. Res. 19 (8), 2478–2486.
Werner, E., Prantl, W., 1990. Slip transfer across grain and phase boundaries. Acta Metallurgica et Materialia 38 (3), 533–537.
Wilkinson, A.J., Randman, D., 2010. Determination of elastic strain fields and geometrically necessary dislocation distributions near nanoindents using electron back scatter diffraction. Philosoph. Mag. 90 (9), 1159–1177.
Wo, P.C., Ngan, A.H.W., 2004. Investigation of slip transmission behavior across grain boundaries in polycrystalline Ni3Al using nanoindentation. J. Mater. Res. 19 (1), 189–201.
Zaeffer, S., Kuo, J.-C., Zhao, Z., Winning, M., Raabe, D., 2003. On the influence of the grain boundary misorientation on the plastic deformation of aluminum bicrystals. Acta Materialia 51 (16), 4719–4735.